ChemComm
Chemical Communications

Accepted Manuscript

This article can be cited before page numbers have been issued, to do this please use: F. Liu, X. Guo, Y. Zhong, S. Fu, J. Li, C. Zhang, H. Zhang, F. Ye, S. Yuan, C. Hu and C. Guo, *Chem. Commun.*, 2024, DOI: 10.1039/D4CC05604C.

ROYAL SOCIETY OF CHEMISTRY

rsc.li/chemcomm

View Article Online
DOI: 10.1039/D4CC05604C

COMMUNICATION

Axial oxygen-bridged FeN_4O/NC produced by ultrafast joule heating for efficient oxygen reduction reaction

Received 00th January 20xx,
Accepted 00th January 20xx

DOI: 10.1039/x0xx00000x

Feng Liu,‡[a] Xinyu Guo,‡[a] Yan Zhong,[a] Shaqi Fu,[a] Jingsha Li,[a] Chunmei Zhang,[a] Heng Zhang,[a] Fenghui Ye,[b] Shuai Yuan,[c] Chuangang Hu*[b] and Chunxian Guo*[a]

Herein, we report an atomically dispersed Fe-N-C catalyst with axial oxygen ligands (FeN_4O/NC) firstly synthesized by ultrafast joule heating. The formation of oxygen species between FeN_4 and graphene, which offers high activity and stability for the ORR. The calculation indicates that FeN_4O/NC offers an optimal adsorption-desorption of oxygen-containing intermediates, providing a promising approach to designing efficient single-atom electrocatalysts.

Electrocatalytic 4e$^-$ oxygen reduction reaction (ORR) is an important process in energy storage and conversion systems, such as metal-air batteries and fuel cells.[1,2] Platinum (Pt)-based catalysts have been widely used to catalyze the ORR. However, high costs and scarce earth abundance of Pt-based catalysts preclude their practical applications in fuel cells.[3,4] Developing highly efficient non-precious ORR catalysts as alternatives to Pt-based catalysts has attracted wide attention.[5-7] Among non-precious ORR catalysts, transition metal, and nitrogen co-doped carbon (M-N-C) single-atom catalysts are regarded as one of the most promising materials owing to their maximum atomic utilization and desired ORR activity.[8-10] In particular, single-atom Fe-N-C catalysts are of great concentration due to their unique electronic structure and impressed catalytic activity.[11-13] Nevertheless, the activity and stability of Fe-N-C catalysts still need to be improved because of the Fe-N_4 moieties with the Fenton effect and a symmetric electron distribution, which are unfavorable for optimizing the adsorption of the ORR intermediates.[14,15]

In recent years, some researchers have reported the axial coordination effect on Fe-N-C catalysts for ORR.[16] For example, Wang et al. found that hydroxy (OH) ligand is part of the active moiety for improving the ORR activity via theoretical calculations.[17] The axial OH ligand can modulate the electronic structure of the Fe atom, resulting in Fe-(OH)N_4 sites facilitating ORR kinetics. In addition, axial OH coordination on the Fe center can increase the adsorption free energy of anion, decrease the H_2O_2 yield of ORR, and hinder the Fenton effect, thus enhancing the durability of the Fe-N-C catalyst.[18] However, most of the electrocatalytic M-N-C catalysts were prepared by tube furnace pyrolysis.[19-21] The metal and carbon precursors would undergo extremely uncontrollable pyrolysis and reconfiguration through tube furnaces with slow heating rates, resulting in complex product structures and possibly different types of active sites. The structure of the active center of the catalyst is not clear enough, which is not conducive to the efficient local regulation of the active center and the accurate study of the structure-activity relationship of the M-N-C catalyst.[22,23] Thus, it is still a challenge to achieve atomically precisely controlled locations of axial ligands on the metal center for efficient ORR.

Herein, we design and synthesize an atomically dispersed Fe-N-C catalyst with axial oxygen ligands (FeN_4O/NC) for ORR by ultrafast joule heating. The aberration-corrected transmission electron microscopy (AC-TEM) and X-ray absorption fine structure (XAFS) analysis reveal that the atomically dispersed Fe atoms exist as axial oxygen coordination FeN_4O/NC species. Benefiting from the unique structure of FeN_4O/NC with suitable adsorption strength of oxygen intermediates on active metal center, the FeN_4O/NC catalyst shows superior ORR activity, of which half-wave potential ($E_{1/2}$) is 0.903 V versus RHE. Notably, the FeN_4O/NC catalyst exhibits excellent durability with only a 7 mV negative shift in $E_{1/2}$ after 10,000 cyclic voltammetry cycles. Density functional theory (DFT) calculations reveal that the axial oxygen ligands in FeN_4O/NC can regulate the electronic structure of the Fe center and adjust the oxygen-containing intermediates adsorption-desorption on the active center, thus resulting in outstanding ORR performance.

[a] *Institute of Materials Science and Devices, School of Materials Science and Engineering, Suzhou University of Science and Technology, Suzhou 215009, China. E-mail: cxguo@usts.edu.cn*
[b] *State Key Laboratory of Organic-Inorganic Composites, College of Chemical Engineering, Beijing University of Chemical Technology, Beijing 100029, China. E-mail: chuangang.hu@mail.buct.edu.cn*
[c] *School of Software and Microelectronics, Peking University, Beijing 102600, China.*
†Electronic Supplementary Information (ESI) available. See DOI: 10.1039/x0xx00000x
‡ These authors contributed equally.

View Article Online DOI: 10.1039/D4CC05000K

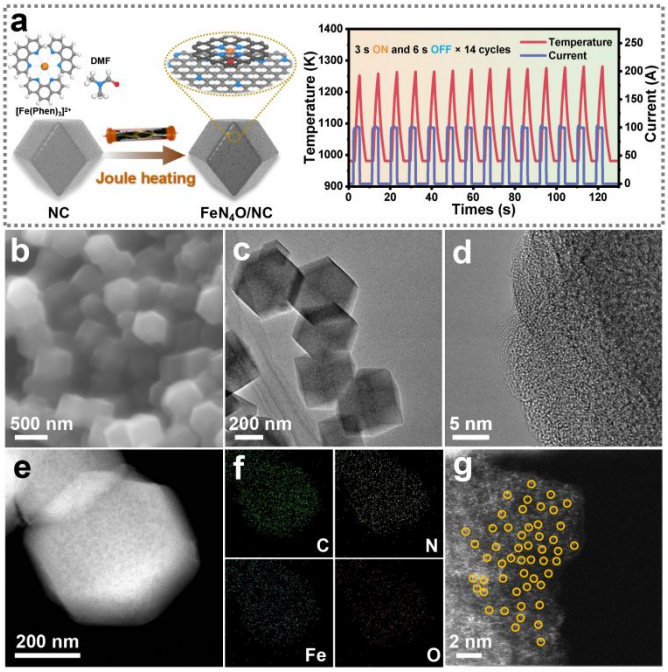

Fig.1 (a) The schematic synthesis illustration of FeN_4O/NC and the temperature-current-time profile of the periodic carbothermal shock treatment process (Input current: 100 A; 3 s-heating and 6 s-cooling is one cycle, a total of 14 cycles, with a maximum temperature of ~1300 K). (b) SEM and (c) TEM images of FeN_4O/NC. (d) HRTEM image of FeN_4O/NC. (e, f) HAADF-STEM and corresponding EDS mapping images of C, N, Fe, and O elements of FeN_4O/NC. (g) AC HAADF-STEM image of FeN_4O/NC.

The ultrafast joule heating method was employed to prepare atomically dispersed Fe-N-C catalysts with axial oxygen ligands (FeN_4O/NC), as schematically illustrated in Fig. 1a (details in the Experimental Section). The ultrafast joule heating process involves 14 carbothermal shock cycles. Each carbothermal shock cycle consists of 3 s of current (100 A)-on heating and 6 s of current (100 A)-off cooling, resulting in a maximum temperature of ~1300 K. Briefly, Fe(II)-phenanthroline complex —$[Fe(Phen)_3]^{2+}$ absorbed with *N, N*-Dimethylformamide (DMF containing oxygen atom) are excited and stripped to form the flow of the single-Fe atoms and CO under the argon joule heating treatment, and simultaneously the single-Fe atoms and CO are trapped and anchored by the defective and nitrogenous sites on the nitrogen-doped carbon (NC) supports to obtain the FeN_4O/NC. Scanning electron microscopy (SEM) and transmission electron microscopy (TEM) images (Fig. 1b and c) present that FeN_4O/NC consists of monodispersed nanoparticles with dodecahedron morphology. In comparison with NC supports, FeN_4O/NC-0.1, FeN_4O/NC-0.3 (i.e. FeN_4O/NC), and FeN_4O/NC-0.5 still maintain the polyhedral architecture and undergoes the ultrafast joule heating process (Figs. S1 amd S2, ESI†). Fig. 1d and Fig. S3 (ESI†) show the high-resolution transmission electron microscopy (HRTEM) and x-ray diffraction (XRD), confirming that no obvious iron and iron oxide nanoparticles were observed in FeN_4O/NC, and the NC supports in FeN_4O/NC were amorphous carbon.

High-angle annular dark-field scanning transmission electron microscope (HAADF-STEM) and corresponding energy-dispersive x-ray spectroscopy (EDS) mapping images for FeN_4O/NC were carried out to display uniform distributions of Fe, N, and O elements over the NC matrix (Fig. 1e and f). The atomically dispersed Fe atoms in FeN_4O/NC can be observed in the aberration-corrected (AC) HADDF-STEM images (Fig. 1g).[22] In addition, the SEM, TEM, HRTEM, and AC HADDF-STEM images for FeN_4/NC were also presented (Fig. S4, ESI†), FeN_4/NC shows the same morphology as FeN_4O/NC and also contains isolated bright spots in AC HADDF-STEM image. N_2 adsorption-desorption isotherms exhibit that the FeN_4O/NC and FeN_4/NC exhibit significant specific surface areas, which are 1235 and 1586 $m^2\ g^{-1}$, respectively (Fig. S5, ESI†). FeN_4O/NC has a similar pore volume to FeN_4/NC (Table S1, ESI†). The release of Zn^{2+} and 2-MIM during the NC formation process can not only increase the porosity, but also expose a number of carbon defects, which contributing to the catalytic activity for FeN_4O/NC. Raman spectra of FeN_4O/NC and FeN_4/NC catalysts show two characteristic peaks at ~1352 and ~1588 cm^{-1}, designated as the D band and G band, respectively (Fig. S6, ESI†). The I_D/I_G ratio for FeN_4O/NC (1.07) was slightly lower than that of the FeN_4/NC (1.09), thus suggesting that the presence of axial oxygen ligands slightly enhanced the graphitization degree of the carbon support.[24]

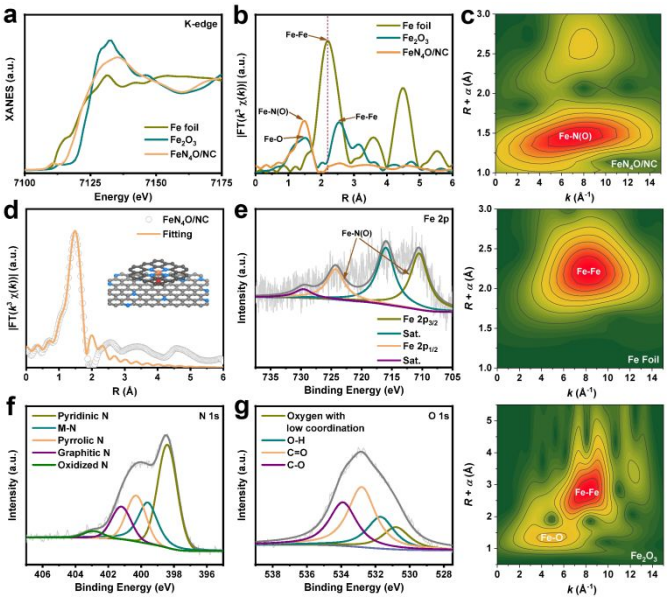

Fig.2 (a) Fe K-edge XANES and (b) Fe K-edge FT-EXAFS spectra for FeN_4O/NC, Fe foil and Fe_2O_3. (c) Wavelet transform (WT)-EXAFS plots for Co element of FeN_4O/NC, Fe foil and Fe_2O_3. (d) FT-EXAFS R-space fitting curve of FeN_4O/NC. High resolution XPS spectra of (e) Fe 2p, (f) N 1s, and (g) O 1s for FeN_4O/NC.

X-ray absorption energy near-edge structure (XANES) and extended X-ray absorption fine structure (EXAFS) spectra were carried out to further study the coordination environment and chemical state of Fe center in FeN_4O/NC. The XANES spectra at the Fe K-edge display that the absorption edge of FeN_4O/NC is located between those of Fe foil and Fe_2O_3 (Fig. 2a), indicating that the Fe atoms exist in a positive oxidation state. EXAFS displays that there is no main peak of the Fe-Fe path in FeN_4O/NC, suggesting the atomically dispersed Fe sites (Fig. 2b). The main peak for FeN_4O/NC located at 1.48 Å, which corresponds to Fe-N(O) coordination. The coordination environment of FeN_4O/NC can be revealed more clearly by the EXAFS wavelet transform (WT) analysis because of its high resolution in both K and R spaces. Fig. 2c presents the maximal WT intensity with the light atom coordination at 1.48 Å in FeN_4O/NC switching to ca. 7.0 $Å^{-1}$, different from Fe foil (8.3 $Å^{-1}$) and Fe_2O_3 (5.0 $Å^{-1}$). The results further verify the individual distribution of Fe sites

View Article Online
DOI: 10.1039/D4CC05604C

and the Fe-N(O) coordination structure. The exact geometry coordination structure of the Fe atom in FeN_4O/NC was acquired by the least-squares EXAFS fitting. Quantitative space spectra fitting confirms the existence of FeN_4O/NC moiety (Fig. 2d and Fig. S7, ESI †).

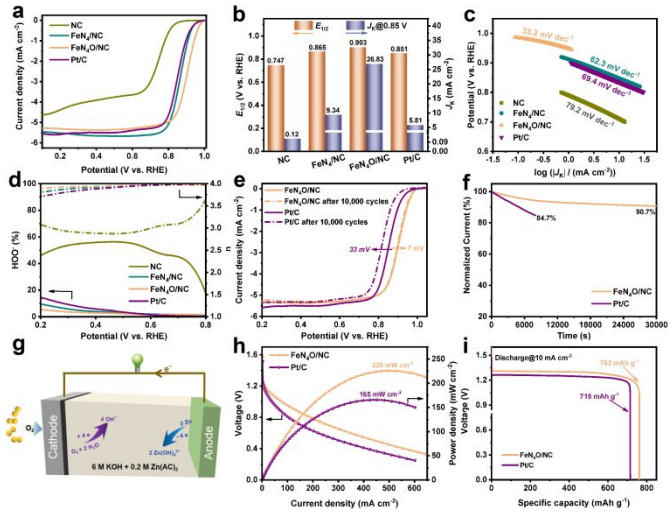

Fig.3 (a) ORR polarization curves of NC, FeN_4/NC, FeN_4O/NC, and Pt/C in O_2-saturated 0.1 M KOH solution with a scan rate of 5 mV S^{-1} and a rotation rate of 1600 rpm. (b) Comparison of $E_{1/2}$ and J_k at 0.85 V for FeN_4O/NC and reference catalysts. (c) Tafel plots and (d) yields of HOO^- and number of transferred electrons (n) of FeN_4O/NC and reference catalysts. (e) ORR polarization curves of FeN_4O/NC and Pt/C catalysts before and after 10,000 CV cycles. (f) Stability test of FeN_4O/NC and Pt/C. (g) Schematic diagram of Zn-air battery. (h) Polarization and power density curves of FeN_4O/NC and Pt/C-based Zn-air batteries. (i) Galvanostatic discharge curves of the Zn-air batteries at 10 mA cm^{-2}.

X-ray photoelectron spectroscopy (XPS) was conducted to analyze the chemical status of samples.[25,26] Table S2 (ESI †) indicates the existence of C, N, O, and Fe elements in samples. Fig. 2e shows the high-resolution XPS Fe 2p spectra for FeN_4O/NC. The main peaks are located at ca. 710.6 eV and 724.3 eV, corresponding to Fe $2p_{3/2}$ and Fe $2p_{1/2}$ for Fe-N/Fe-O bond, respectively. Compared to the peak of Fe $2p_{3/2}$ for FeN_4/NC (710.5 eV) (Fig. S8, ESI†), the peak of Fe $2p_{3/2}$ for FeN_4O/NC exhibits a up-shift by 0.1 eV, which is presumably induced by axial oxygen ligands. The high-resolution XPS C 1s spectra of FeN_4O/NC and FeN_4/NC can be deconvoluted into three peaks at 284.8, 286.6, and 288.7 eV, which correspond to C-C, C-N, and C-O, respectively (Fig. S9, ESI †). The N 1s spectrum of FeN_4O/NC was divided into pyridinic N (~398.4 eV), metal-N (~399.2 eV), pyrrolic N (~400.6 eV), graphitic N (~401.2 eV), and oxidized N (~402.9 eV), respectively (Fig. 2f). Oxidized N was not found in N 1s spectra of FeN_4/NC (Fig. S10, ESI†). The fitted peak for the Fe-N bond is consistent with the analysis of XAS. Meanwhile, as shown in Fig. 2g and Fig. S11 (ESI†), high-resolution XPS O 1s spectra for FeN_4O/NC and FeN_4/NC exhibit that the intense peak for low coordination oxygen can be observed in FeN_4/NC, and decreases in FeN_4O/NC.

The electrocatalytic ORR performance of the FeN_4O/NC and FeN_4/NC catalysts was studied by the rotating disk electrode (RDE) measurements. The optimal ORR catalyst (FeN_4O/NC) were derived from $[Fe(Phen)_3]^{2+}$/NC by adjusting with different $[Fe(Phen)_3]^{2+}$ addition (Fig. S12 and Table S3, ESI†). The linear sweep voltammetry (LSV) analysis exhibits that FeN_4O/NC displays a favorable ORR activity with a half-wave potential ($E_{1/2}$) of 0.903 V (versus RHE), which is more positive than that of commercial Pt/C and higher than those of most of previously reported highly active non-precious metal catalysts (Fig. 3a and Table S4, ESI†). FeN_4O/NC exhibits the highest J_k@0.85 value (26.83 mA cm^{-2}), which is higher than those of NC (0.12 mA cm^{-2}), FeN_4/NC (9.34 mA cm^{-2}), and Pt/C (5.81 mA cm^{-2}), respectively (Fig. 3b). Fig. 3c shows a low Tafel slope of 33.2 mV dec^{-1} for FeN_4O/NC, which is lower than those of NC (79.2 mV dec^{-1}), FeN_4/NC (62.3 mA cm^{-2}) and Pt/C (69.4 mV dec^{-1}), indicating that FeN_4O/NC has the faster reaction kinetics.[27] FeN_4O/NC presents mass activity of 11.75 and 7.28 mA mg^{-1} at 0.85 and 0.90 V (Fig. S13, ESI†), respectively, which are 1.27 and 2.17 times higher than those of FeN_4/NC. As shown in Fig. 3d, FeN_4O/NC gives a low yield of HOO^- (below 5%) in a potential range of 0.2-0.8 V. The electron transfer number (n) for FeN_4O/NC is close to 4.0, which is in agreement with the linear Koutecky-Levich (K-L) plots obtained from RDE measurements at different rotation speeds (Fig. S14, ESI†), indicating the four-electron transfer pathway toward ORR for FeN_4O/NC. Furthermore, FeN_4O/NC exhibits a higher electrochemical double-layer capacitance (C_{dl}) of 27.7 mF cm^{-2} than that of FeN_4/NC (22.9 mF cm^{-2}), suggesting that the axial oxygen ligands synergistic FeN_4 sites are conducive to improve the electrochemically active surface area (ESCA) (Fig. S15, ESI †).[28] Impressively, FeN_4O/NC exhibits outstanding durability than the Pt/C catalyst, as observed by slighter decay in $E_{1/2}$ during the accelerated stability test (ADT) (Fig. 3e) and the lower decay in the chronoamperometry measurement (Fig. 3f). FeN_4O/NC after durability test still maintains the dodecahedron morphology and atomically dispersed Fe atoms (Fig. S16, ESI†). Fig. S17 (ESI †) shows that FeN_4O/NC presents excellent methanol resistance, as confirmed by that the current density of FeN_4O/NC does not decay after injecting methanol into the electrolyte. The primary Zn-air battery (ZAB) was assembled by using FeN_4O/NC as the air cathode electrocatalyst and zinc foil as the anode, of which schematic diagram is shown in Fig. 3g. The FeN_4O/NC-based ZAB exhibits a higher stable open-circuit voltage of 1.46 V than that of commercial Pt/C (1.42 V) used as a reference (Fig. S18, ESI†). As shown in Fig. 3h, the FeN_4O/NC-based ZAB shows an excellent peak power density of 226 mW cm^{-2}, which is higher than that of commercial Pt/C-based ZAB (165 mW cm^{-2}). Furthermore, the FeN_4O/NC-based ZAB shows an ultra-high specific discharge capacity of 762 mAh g^{-1} at a discharge current density of 10 mA cm^{-2}, which is higher than that of commercial Pt/C-based ZAB (715 mAh g^{-1}) (Fig. 3i).

To further reveal the effects of axial oxygen ligands on the properties of FeN_4 sites as well as their enhanced ORR activity, two models (FeN_4/NC and FeN_4O/NC) with the typical four-electron transfer pathway toward ORR were constructed for DFT calculations (Fig. 4a and b). Fig. 4c and Fig. S19 (ESI†) present the Gibbs free-energy diagrams of the reduction of O_2 to OH^- on the FeN_4O/NC and FeN_4/NC active sites. The Gibbs free-energy diagrams of ORR on both FeN_4O/NC and FeN_4/NC exhibit a downhill pathway at zero electrode potential (U = 0 V vs RHE), suggesting the exothermic nature of all the elementary steps. At U = 1.23 V, the last elementary step of the ORR for both FeN_4O/NC and FeN_4/NC models possesses the highest free energy difference, indicating that the rate-determining step (RDS) is the reduction of OH* to OH^- ($OH^* + 3OH^- + e^- \rightarrow 4OH^- + *$). The free energy change of the RDS for FeN_4O/NC is calculated to be the ORR overpotential (η_{ORR}) value of 0.41 V, which is much smaller than that of FeN_4/NC (0.64 V) (Fig. 4d). The lower

overpotential for the FeN_4O/NC model implies that the FeN_4O/NC site is thermodynamically favorable during the ORR process. Impressively, as can be seen in Fig. 4d, the thermodynamic limiting potential of FeN_4O/NC is up to 0.82 V, which is higher than that of FeN_4/NC (0.59 V), which can further demonstrate that FeN_4O/NC has an excellent electrocatalytic activity toward ORR. The adsorption energy of O on the FeN_4O/NC is lower than that of FeN_4/NC (Fig. S20, ESI †), suggesting the weakened adsorption of O-containing intermediates and high electrocatalytic ORR kinetics at the FeN_4O/NC site.

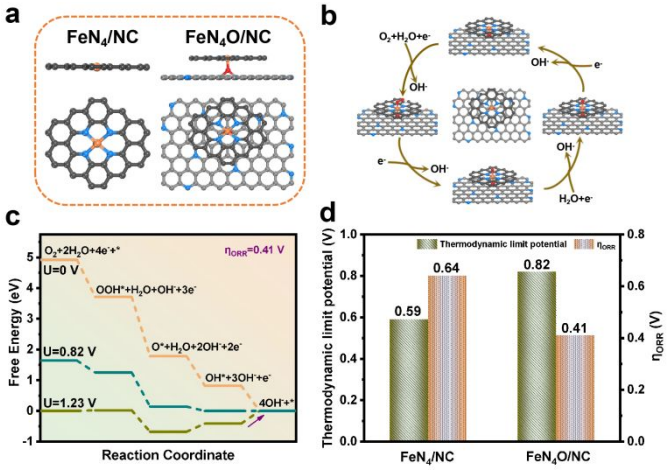

Fig.4 (a) Atomic structure of FeN_4/NC and FeN_4O/NC sites. (b) Proposed ORR mechanism on the FeN_4O/NC catalyst. (c) Free-energy diagram of ORR for FeN_4O/NC model. (d) Thermodynamic limiting potential and η_{ORR} of FeN_4/NC and FeN_4O/NC sites.

In summary, the axial oxygen-bridged FeN_4O/NC catalyst was successfully prepared by ultrafast joule heating for ORR. Benefiting from the rational construction of active sites, the FeN_4O/NC catalyst exhibited excellent ORR activity and stability. Both experimental analyses and theoretical calculations reveal that the axial oxygen ligands synergistic FeN_4 sites in FeN_4O/NC have optimal adsorption-desorption of ORR oxygen-containing intermediates, thus enhancing ORR performance. Overall, our study not only provides a new approach for regulating the microenvironment of single-atom catalysts but also offers a new opportunity for developing highly efficient catalysts for wide applications in energy conversion and storage.

This work was financially supported by the National Natural Science Foundation of China (22372113), the National Key Research and Development Program of China (2021YFA0910403), the Natural Science Foundation of Jiangsu Province (BK20240995), and the Natural Science Research Project of Higher Education Institutions in Jiangsu Province (24KJB530020).

Data availability

The data that support the findings of this study are available from the corresponding author upon reasonable request.

Conflicts of interest

There are no conflicts to declare.

Notes and references

View Article Online
DOI: 10.1039/D4CC05604C

1 A. Mehmood, M. Gong, F. Jaouen, A. Roy, A. Zitolo, A. Khan, M. T. Sougrati, M. Primbs, A. M. Bonastre, D. Fongalland, G. Drazic, P. Strasser and A. Kucernak, *Nat. Catal.*, 2022, **5**, 311-323.
2 G. Wu, K. L. More, C. M. Johnston and P. Zelenay, *Science*, 2011, **332**, 443-447.
3 M. Qiao, Y. Wang, Q. Wang, G. Hu, X. Mamat, S. Zhang and S. Wang, *Angew. Chem. Int. Ed.*, 2020, **59**, 2688-2694.
4 G. Xing, M. Tong, P. Yu, L. Wang, G. Zhang, C. Tian and H. Fu, *Angew. Chem. Int. Ed.*, 2022, **61**, e202211098.
5 C. Zhao, W. Luo, H. Tian, T. Lu, L. Yi, Y. Zhang, L. Shi and Y. Ma, *Chem. Commun.*, 2023, **59**, 6749-6752.
6 L. Jiao and H.L. Jiang, *Chem*, 2019, **5**, 786-804.
7 F. Liu, L. Shi, X. Lin, B. Zhang, Y. Long, F. Ye, R. Yan, R. Cheng, C. Hu, D. Liu, J. Qiu and L. Dai, *Sci. Adv.*, 2023, **9**, eadg0366.
8 J. Huang, Q. Zhang, J. Ding and Y. Zhai, *Mater. Rep.: Energy*, 2022, **2**, 100141.
9 J. Liu, J. Jia, H. Wen, S. Li, Y. Wu, Q. Wang, Z. Kan, Y. Li, X. Wu, J. Zhao, S. Liu and B. Li, *Chem. Commun.*, 2023, **59**, 3550-3553.
10 L. Shi, D. Liu, X. Lin, R. Cheng, F. Liu, C. Kim, C. Hu, J. Qiu, R. Amal and L. Dai, *Adv. Mater.*, 2024, **36**, 2314077.
11 Y. Jia, X. Xiong, D. Wang, X. Duan, K. Sun, Y. Li, L. Zheng, W. Lin, M. Done, G. Zhang, W. Liu and X. Sun, *Nano-Micro Lett.*, 2020, **12**, 116.
12 F. Abdelghafar, X. Xu, S. P. Jiang and Z. Shao, *Mater. Rep.: Energy*, 2022, **2**, 100144.
13 F. Liu, L. Shi, S. Song, K. Ge, X. Zhang, Y. Guo and D. Liu, *Small*, 2021, **17**, 2102425.
14 F. Liu, Y. Guo, Y. Zhong, J. Li, H. Zhang, L. Shi, X. Lin, F. Ye, K. Ge, S. Yuan, C. Hu and C. Guo, *Chem. Commun.*, 2024, **60**, 4064-4067.
15 X. Cheng, X. Jiang, S. Yin, L. Ji, Y. Yan, G. Li, R. Huang, C. Wang, H. Liao, Y. Jiang and S. Sun, *Angew. Chem. Int. Ed.*, 2023, **62**, e202306166.
16 L. Li, B. Huang, X. Tang, Y. Hong, W. Zhai, T. Hu, K. Yuan and Y. Chen, *Adv. Funct. Mater.*, 2021, **31**, 2103857.
17 Y. Wang, Y. J. Tang and K. Zhou, *J. Am. Chem. Soc.*, 2019, **141**, 14115.
18 F. Wang, Y. Zhou, S. Lin, L. Yang, Z. Hu and D. Xie, *Nano Energy*, 2020, **78**, 105128.
19 Y. Guo, X. Wang, L. Feng, F. Liu, J. Liang, X. Wang and X. Zhang, *Green Chem.*, 2023, **25**, 3585-3591.
20 Y. Li, Z. He, F. Wu, S. Wang, Y. Cheng and S. Jiang, *Mater. Rep.: Energy*, 2023, **3**, 100197.
21 Y. Guo, F. Liu, L. Feng, X. Wang, X. Zhang and J. Liang, *Chem. Eng. J.*, 2022, **429**, 132150.
22 X. Li, T. Chen, B. Yang and Z. Xiang, *Angew. Chem. Int. Ed.*, 2023, **135**, e202215441.
23 P. Peng, L. Shi, F. Huo, C. Mi, X. Wu, S. Zhang and Z. Xiang, *Sci. Adv.*, 2019, **5**, eaaw2322.
24 F. Liu, L. Shi, X. Lin, D. Yu, C. Zhang, R. Xu, D. Liu, J. Qiu and L. Dai, *Appl. Catal. B Environ.*, 2022, **302**, 120860.
25 Y. Zhao, H. Cui, Y. Hu, S. Li, F. Liu, B. Shen, K. Ge, B. Liu and Y. Yang, *Appl. Catal. B Environ.*, 2025, **361**, 124567.
26 Q. Hu, S. Qi, Q. Huo, Y. Zhao, J. Sun, X. Chen, M. Lv, W. Zhou, C. Feng, X. Chai, H. Yang and C. He, *J. Am. Chem. Soc.*, 2024, **146**, 2967-2976.
27 L. Jing, W. Wang, Q. Tian, Y. Kong, X. Ye, H. Yang, Q. Hu and C. He, *Angew. Chem. Int. Ed.*, 2024, e202403023.
28 X. Lin, X. Li, L. Shi, F. Ye, F. Liu and D. Liu, *Small*, 2024, **20**, 2308517.

View Article Online
DOI: 10.1039/D4CC05604C

Data available on request from the authors.

The data that support the findings of this study are available from the corresponding author, Chunxian Guo, upon reasonable request.